Receptivity of Supersonic Boundary Layers Due To Acoustic Disturbances Over Blunt Cones

P.Balakumar

NASA Langley Research Center, Hampton, VA 23681

Receptivity and stability of supersonic boundary layers over a 5-degree straight cone with a blunt tip are numerically investigated at a free stream Mach number of 3.5 and at a high Reynolds number of 10^6/inch. Both the steady and unsteady solutions are obtained by solving the full Navier-Stokes equations using the 5th-order accurate weighted essentially non-oscillatory (WENO) scheme for space discretization and using third-order total-variation-diminishing (TVD) Runge-Kutta scheme for time integration. The linear stability results showed that bluntness has less stabilizing effects on the stability of boundary layers over cones than on flat plates and wedges. The unsteady simulations of the interaction of plane three-dimensional acoustic waves with the cone showed that the modulation of wavelength and the generation of instability waves first occurred near the leading edge in the plane where the constant acoustic phase lines are perpendicular to the cone axis. Further downstream, this instability region spreads in the azimuthal direction from this plane.

Introduction

This paper is concerned with the receptivity and the stability of supersonic boundary layers over blunt axi-symmetric cones at zero angles of attack. It is now understood that transition from a laminar to a turbulent state originates from the internalization of external disturbances into the boundary layer (receptivity) and the exponential growth (linear instability) of these internalized disturbances inside the boundary layer. The second process is governed by the linearized stability equations. The stability characteristics of compressible boundary layers have been thoroughly investigated[1]. The supersonic boundary layers are unstable to three-dimensional disturbances called the first mode. The phase velocity of the unstable first mode disturbances increases from $U_\infty - a_\infty$ near the lower neutral point to C_s near the upper neutral point, where U_∞ is the free stream velocity, a_∞ is the free stream acoustic velocity and C_s is the mean velocity at which the generalized inflection point occurs. The unstable region and the amplification rate of the disturbances depend on the flow parameters, Mach number and unit Reynolds number, on the geometry, bluntness and wall condition, and on the frequency and the orientations of the disturbances. However, when these conditions are known the computations of the boundary layers and the stability characteristics can be performed without much difficulty.

The first process is called receptivity and it depends on several parameters including the flow features near the leading edge, the stability characteristics of the boundary layers and the types of external disturbances that impinge on the boundary layer. Since the phase speed of the acoustic disturbances synchronizes with the phase speed of the first modes near the lower branch of the neutral stability curve it is expected that acoustic disturbances will be very efficient in generating the instability waves in supersonic boundary layers. This observation led to numerous investigations on the interactions of acoustic waves with supersonic boundary layers. The investigations can be divided into two groups. One is the forced response of the parallel and non-parallel boundary layers to free stream acoustic disturbances[2, 3, 4, 5]. In these studies, it was found that acoustic waves excite disturbances inside the boundary layer that are much larger than those in the free stream. The computations also revealed that at

some critical Reynolds numbers the incoming acoustic waves are completely absorbed by the boundary layer. It was postulated that the first mode emerges downstream of this region with the initial amplitude given by the forced response calculations. The second group of investigations are concerned with the generation of the first and the second modes near the leading edge region due to the interaction with the free stream acoustic disturbances[6, 7, 8, 9]. Fedorov and Khokhlov[6] investigated the excitation of the first and the second modes by the longitudinal acoustic waves using asymptotic theory. They showed that the growing boundary layer diffracts the incoming acoustic wave and generates eigen solutions inside the boundary layer. In a companion paper[7] they investigated the generation of the instability waves due to incoming acoustic waves at finite angles of incidence. It was identified that at small incidence angles the incident and the reflected waves are diffracted by the boundary layer resulting in the formation of the eigen solutions. At large incidence angles the scattered acoustic waves near the leading edge are diffracted by the boundary layer resulting in the generation of the eigen solutions. The receptivity of supersonic boundary layers is investigated numerically[8] by imposing a periodic Mach wave near the leading edge of the lower surface of a flat plate. It was shown that the first mode instability waves are generated in the upper surface of the flat plate and forced response was created in the lower side.

At high Reynolds numbers the neutral point is located very close to the leading edge within one wavelength of the acoustic wave and the synchronization of the acoustic wave and the first mode occurs closer than this. Hence the flow features near the leading edge such as effects of bluntness; shocks and non-parallelism may become very important in the generation of the instability waves. These effects were not included in the aforementioned analysis or in the computations. In our previous studies[10, 11, 12], the generation and the evolution of three-dimensional disturbances induced by slow and fast acoustic disturbances and isolated roughness in a supersonic boundary layer over blunt flat plates and wedges at a free stream Mach number of 3.5 were numerically investigated by solving the full three-dimensional Navier-Stokes equations. It was found that instability waves are generated within one wavelength of the acoustic wave from the leading edge. The wavenumber first decreases from the acoustic value and then slowly increases to the instability wave value, which is smaller than the acoustic wavenumber. The computed receptivity coefficients based on the pressure fluctuations at the wall near the neutral points are about 1.20 and 0.07 for the slow and the fast acoustic waves respectively.

Most of the receptivity analysis and computations are performed for flows over flat plates. Since the mean flow is uniform in the spanwise direction one Fourier mode with constant spanwise wavelength is considered in the analysis. In flows over axi-symmetric geometries the azimuthal wavenumber has to be an integer due to the circular periodicity in the azimuthal direction. These azimuthal wavenumbers for the unstable waves in supersonic boundary layers are large in the order of 10 to 30. When these wavenumbers are converted to wavelengths by dividing the circumferential length by the wavenumber, the wavelengths become very small near the nose and increase gradually in the axial direction. It was found in an earlier investigation[10] of receptivity of supersonic boundary layers to acoustic disturbances over flat plates that the instability waves are generated near the leading edge. The question is then how do the acoustic disturbances in the free stream with long spanwise wavelengths generate these small wavelengths or the large wavenumber disturbances inside the boundary layer over axi-symmetric bodies.

There were several relevant transition experiments performed at NASA Langley in the Mach 3.5 Supersonic Low-Disturbance tunnel. Boundary-layer transition data on a flat plate and on a cone along with free stream noise levels and the power spectral distribution of the free stream noise are presented in Ref. 13. As a first step, the computations are performed for the same conditions as in the experiment. The objectives are to understand the receptivity process near the leading edge of an axi-symmetric cone and to estimate the receptivity coefficient of the instability waves generated near the leading edge. A schematic diagram of the computational set up is depicted in Fig. 1.

Governing Equations.

The equations solved are the three-dimensional unsteady compressible Navier-Stokes equations in conservation form in cylindrical coordinates

$$\frac{\partial}{\partial t}Q + \frac{\partial F}{\partial x} + \frac{\partial G}{\partial r} + \frac{1}{r}\frac{\partial H}{\partial \theta} = \frac{1}{r}S. \tag{1}$$

$$Q = \begin{bmatrix} \rho \\ \rho u \\ \rho v \\ \rho w \\ \rho E \end{bmatrix}$$

$$F = \begin{bmatrix} \rho u \\ p + \rho u^2 - \tau_{xx} \\ \rho uv - \tau_{xr} \\ \rho uw - \tau_{x\theta} \\ (\rho E + p)u - u\tau_{xx} - v\tau_{xr} - w\tau_{x\theta} - k\frac{\partial T}{\partial x} \end{bmatrix} \qquad G = \begin{bmatrix} \rho v \\ \rho uv - \tau_{xr} \\ p + \rho v^2 - \tau_{rr} \\ \rho vw - \tau_{r\theta} \\ (\rho E + p)v - u\tau_{xr} - v\tau_{rr} - w\tau_{r\theta} - k\frac{\partial T}{\partial r} \end{bmatrix}$$

$$H = \begin{bmatrix} \rho w \\ \rho uw - \tau_{x\theta} \\ \rho vw - \tau_{r\theta} \\ p + \rho w^2 - \tau_{\theta\theta} \\ (\rho E + p)w - u\tau_{x\theta} - v\tau_{r\theta} - w\tau_{\theta\theta} - \frac{k}{r}\frac{\partial T}{\partial \theta} \end{bmatrix} \qquad S = \begin{bmatrix} -\rho v \\ -\rho uv + \tau_{xr} \\ -\rho v^2 + \tau_{rr} + \rho w^2 - \tau_{\theta\theta} \\ -2\rho vw + 2\tau_{r\theta} \\ -(\rho E + p)v + u\tau_{xr} + v\tau_{rr} + w\tau_{r\theta} + k\frac{\partial T}{\partial r} \end{bmatrix}$$

Here (x, r, θ) are the cylindrical coordinates, (u, v, w) are the velocity components, ρ is the density, and p is the pressure. E is the total energy given by

$$E = e + \frac{u^2 + v^2 + w^2}{2},$$

$$e = c_v T, \quad p = \rho RT. \tag{3}$$

Here e is the internal energy and T is the temperature. The shear stresses are given by

$$\tau_{xx} = \frac{2}{3}\mu\left(2\frac{\partial u}{\partial x} - \frac{v}{r} - \frac{\partial v}{\partial r} - \frac{1}{r}\frac{\partial w}{\partial \theta}\right)$$

$$\tau_{rr} = \frac{2}{3}\mu\left(2\frac{\partial v}{\partial r} - \frac{v}{r} - \frac{\partial u}{\partial x} - \frac{1}{r}\frac{\partial w}{\partial \theta}\right)$$

$$\tau_{\theta\theta} = \frac{2}{3}\mu\left(\frac{2}{r}\frac{\partial w}{\partial \theta} + 2\frac{v}{r} - \frac{\partial u}{\partial x} - \frac{\partial v}{\partial r}\right)$$

$$\tau_{xr} = \mu\left(\frac{\partial u}{\partial r} + \frac{\partial v}{\partial x}\right)$$

$$\tau_{x\theta} = \mu\left(\frac{1}{r}\frac{\partial u}{\partial \theta} + \frac{\partial w}{\partial x}\right)$$

$$\tau_{r\theta} = \mu\left(\frac{1}{r}\frac{\partial v}{\partial \theta} + \frac{\partial w}{\partial r} - \frac{w}{r}\right)$$

(4)

The viscosity (μ) is computed using Sutherland's law and the coefficient of conductivity (k) is given in terms of the Prandtl number Pr. The variables ρ, p, T and velocity are non-dimensionalized by their corresponding reference variables ρ_∞, p_∞, T_∞ and $\sqrt{RT_\infty}$ respectively. The reference value for length is computed by $\sqrt{vx_0/U_\infty}$, where x_0 is a reference location. For the computation, the equations are transformed from the physical coordinate system (x, r, θ) to the computational curvilinear coordinate system (ξ, η, ζ) in a conservative manner. The corresponding Cartesian coordinates are (x, y, z) with z and y-axis oriented along $\theta = 0$ and 90 degree lines respectively, Fig. (1).

Solution Algorithm

The governing equations are solved using a 5th order accurate weighted essentially non-oscillatory (WENO) scheme for space discretization and using a third order, total variation diminishing (TVD) Runge-Kutta scheme for time integration. These methods are suitable in flows with discontinuities or high gradient regions. The governing equations are solved discretely in a uniform structured computational domain where flow properties are known point wise at the grid nodes. In a given direction, the spatial derivatives are approximated to a higher order at the nodes, using the neighboring nodal values in that direction. The resulting equations are then integrated in time to get the point values as a function of time. Since the spatial derivatives are independent of the coordinate directions, multi dimensions can be easily added to the method. It is well known that approximating a discontinuous function by a higher order (two or more) polynomial generally introduces oscillatory behavior near the discontinuity, and this oscillation increases with the order of the approximation. The essentially non-oscillatory (ENO) and the improvement of this, WENO methods, were developed to maintain the higher order approximations in the smooth regions and to eliminate or suppress the oscillatory behavior near the discontinuities. These are achieved by systematically adopting or selecting the stencils based on the smoothness of the function that is being approximated. Reference 14 explains the WENO and the TVD methods and the formulas. Reference 15 gives the application of the ENO method to the N-S equations. Reference 16 describes in detail the solution method implemented in this computation.

At the outflow boundary, characteristic boundary conditions are used. At the wall, viscous conditions are used for the velocities and a constant temperature condition is employed for the temperature. The density at the wall is computed from the continuity equation. In the azimuthal direction, symmetric and

periodic conditions are used at the boundaries. In the mean flow computations, the free-stream values are prescribed at the upper boundary that lies outside the bow shock. In the unsteady computations, the acoustic perturbations are superimposed 0n the uniform mean flow at the upper boundary. The procedure is to first compute the steady mean flow by performing unsteady computations using a variable time step until the maximum residual reaches a small value $\sim 10^{-11}$. A CFL number of 0.15 is used near the nose region and 0.50 is used downstream. The next step is to introduce unsteady disturbances at the upper boundary of the computational domain and to perform time accurate computations to investigate the interaction and evolution of these disturbances downstream. There exists a singularity along the symmetry axis $r = 0$. This singularity is removed by taking the limit of the governing equations at $r = 0$.

The symmetric acoustic field that impinges on the outer boundary is taken to be in the following form.

$$
\begin{aligned}
p'_{ac} &= \text{Real}\left\{ \tilde{p}_{ac} e^{i\alpha_{ac}x \pm i\beta_{ac}z + i\varepsilon_{ac}y - i\omega t} \right\} \\
&+ \text{Real}\left\{ \tilde{p}_{ac} e^{i\alpha_{ac}x \pm i\beta_{ac}z - i\varepsilon_{ac}y - i\omega t} \right\}.
\end{aligned}
\tag{7}
$$

Here α_{ac}, β_{ac}, ε_{ac} are the acoustic wavenumbers, and ω is the frequency of the acoustic disturbance. The wavenumber in the y-direction ε_{ac} determines the incident angle of the acoustic waves and in this paper computations are performed for zero incident angle, $\varepsilon_{ac} = 0.0$.

Results

Computations are performed for supersonic flows over a 5-degree half-angle cone with blunt leading edges. Table 1 gives the flow parameters and Fig. 1 shows the schematic diagram of the computational set up. The nose region of the wedge is modeled as a circle of the form

$$
(x - r_0)^2 + y^2 = r_0^2.
\tag{8}
$$

Here r_0 is the radius of the leading edge bluntness. The circular nose is smoothly merged with the cone by a tenth order polynomial. Unsteady simulations are performed for nose radii $r_0 = 0.001$ and 0.01 inches at a unit Reynolds number of $1.0*10^6$/inch. Stability computations also are performed for nose radius $r_0 = 0.001$, 0.01 and 0.05 inches to investigate the effects of bluntness on the instability of supersonic boundary layers over axi-symmetric bodies. These parameters give the Reynolds numbers based on the nose radius equal to 10^3, 10^4 and $5*10^4$.

Table 1 Flow parameters for the wind tunnel model

Free stream Mach number: M_∞=3.5

Free stream Reynolds number: Re_∞=1.0*10^6/in.

Free stream density: ρ_∞=2.249*10^{-2} lbm/ft^3

Free stream pressure: p_∞=187.74 lbf/ft^2

Free stream velocity: U_∞=2145.89 ft/s

Free stream temperature: T_∞=156.42 $^\circ$R

Free stream kinematic viscosity: ν_∞=1.7882*10^{-4} ft^2/s

Wall temperature: = adiabatic condition

Prandtl number: $Pr = 0.72$

Ratio of specific heats: $\gamma = 1.4$

Length scale $\sqrt{\dfrac{v_\infty x_0}{U_\infty}} = 5.892 * 10^{-5}$ ft. ($x_0 = 0.5$ in.)

The boundary layer thickness at $x_0 = 0.5$ in.: $\delta_0 = .0055$ in.

Non–dimensional frequency $F = 1 * 10^{-5}$ is equivalent to 41.0 kHz

The non-dimensional frequency F is defined as $F = \dfrac{2\pi v_\infty f}{U_\infty^2}$,

where f is the frequency in Hertz.

The grid is generated using analytical formulae. The grid stretches in the η direction close to the wall and is uniform outside the boundary layer. In the ξ direction, the grid is symmetric about the leading edge and very fine near the nose and is uniform in the flat region. The grid is uniform in the azimuthal direction. The outer boundary outside of the shock follows a circle near the nose region with its vertex located a short distance upstream of the nose and follows a parabola downstream of the nose to capture the boundary layer accurately. The computational domain extends from $x = -0.015$ to 10.0 inches in the axial direction. Calculations were performed using a grid size (2001*251*91) and (3001*351*136) depending on the wavelength of the acoustic disturbances. Due to the very fine grid requirement near the nose, the allowable time step is very small and the computations become very expensive to simulate the unsteady computations in the entire domain at once. To overcome this, calculations are performed in two steps. First, the computations are done near the nose region with a very small time step. Second, the flow properties in the middle of this domain are fed as inflow conditions for the second larger domain and the computations are carried out with a larger time step.

Linear instability

The local linear parallel stability analysis is performed for the axi-symmetric similarity boundary layers over the 5-degree half angle cone at a free stream Mach number of 3.5. The conditions downstream of the shock on the surface of the cone are:

$$
\begin{aligned}
M_s &= 3.355 \\
T_s &= 1.06\, T_\infty \\
\rho_s &= 1.15\, \rho_\infty \\
p_s &= 1.16\, p_\infty \\
Re_s/in &= 1.075 * 10^6
\end{aligned}
$$

Here, M_s, T_s, ρ_s and p_s are the inviscid surface Mach number, temperature, density, and the pressure respectively. Two forms of disturbances are used to perform the stability computations.

$$\phi(r,x,z,t) = \tilde{\phi}(r)\, e^{i\alpha s + i\beta z - i\omega t}$$

$$\phi(r,x,\theta,t) = \tilde{\phi}(r)\, e^{i\alpha s + im\theta - i\omega t}$$

In the first form, β represents the spanwise wavenumber and in the second form m, which is an integer, represents the azimuthal wavenumber. The wavenumbers β and m are related by the relation

$$\beta = \frac{m}{R}$$

where R is the radius of the surface. Hence if one assumes a constant β, the azimuthal wavenumber m will vary along the axial direction and if m is assumed to be a constant the spanwise wavenumber β will vary along the axis. In axi-symmetric boundary layers the mathematically correct form for the disturbance is the second equation. However, if one neglects the curvature effects in the local stability analysis both forms will yield the same stability results. As the equation shows, near the nose region where the radius of the cone approaches zero the wavenumber β becomes very large or the spanwise wavelength becomes very small. These observations are very important when one investigates the receptivity of instability waves due to external disturbances in axi-symmetric boundary layers. How do the external acoustic disturbances with large spanwise wavelengths generate these very small wavelength instability waves near the leading edge? The possibilities are that the spanwise acoustic waves are modulated near the sharp nose region and the instability waves are generated in this region or the acoustic waves interact with small roughness near the nose region and the instability waves are generated. In this paper we consider the first possibility and investigate the interaction of acoustic waves with a cone in supersonic boundary layers.

The linear stability results and the N-Factor computations for the similarity boundary layer over the 5-deg cone are shown in figures 2 and 3. Figure 2 (a) shows the neutral stability diagram for different wave angles 0, 45, 60 and 70 degrees in the $\left(F, \sqrt{\mathrm{Re}_x}\right)$ plane. Figures 2(b) and (c) show the N-Factor diagrams for the most amplified frequencies. Figure 2(b) shows the results for constant non-dimensional spanwise wave numbers β and figure 2(c) shows the results for constant azimuthal wave numbers m. The most amplified frequency is about $F = 2.0\text{-}2.5*10^{-5}$ and the spanwise wave number of the most amplified wave is about $\beta = 0.05$. The azimuthal wave number of the most amplified wave is about $m = 20$. In the experiment the transition occurred at a Reynolds number of 3000 and this yields an N-Factor of 10 for a constant β and a factor of 8.5 for a constant m. The critical Reynolds number is about 700 and the critical Reynolds number for the most amplified disturbances is about 1000. To understand the length scales involved it is better to provide the wavenumbers in dimensional quantities. Figures 3(a) and (b) show the variation of the axial and spanwise wavelengths $\left(\lambda_x, \lambda_z\right)$ in inches and the growth rates $\left(-\alpha_i\right)$ for the most amplified wave with the frequency $F = 2.0*10^{-5}$. Figure 3(a) shows the results for a constant spanwise wave number of $\beta = 0.05$ and figure 3(b) shows the results for constant azimuthal wave numbers of $m = 10$ and 20. The non-dimensional spanwise wavenumber $\beta = 0.05$ corresponds to a dimensional wavelength of 0.089 inches. Figure 3a shows that for a constant $\beta = 0.05$ the wavenumber m varies from 3 at a Reynolds number of 700 to about 50 at a Reynolds number of 3000. The axial wavelength λ_x increases from 0.168 inches to 0.210 inches and the waveangle increases from 60 to 65 degrees. Figure 3(b) shows that for a constant azimuthal wavenumber of $m = 10$ the spanwise wavelength increases from 0.032 inches to 0.46 inches and the axial wavelength first decreases from 0.20 inches to 0.183 inches and then increases to 0.212 inches. The waveangle decreases from 80 to 20 degrees. For a constant spanwise wave number of $m = 20$ the spanwise wavelength increases from 0.016 inches to 0.23 inches and the axial wavelength first decreases from 0.23 inches to 0.192 inches and then increases to 0.207 inches. The waveangle decreases from 85 to 40 degrees.

Acoustic waves

The governing equations and the solutions for plane acoustic waves are given in Ref. 10. The acoustic pressure p is in the form

$$p = \tilde{p}_{ac} e^{i(\alpha_{ac}x + \varepsilon_{ac}y + \beta_{ac}z - \omega t)}.$$

The dispersion relation among the acoustic wavenumbers α_{ac}, β_{ac}, ε_{ac} and the frequency ω is given by

$$(\alpha_{ac}U_0 - \omega)^2 = (\alpha_{ac}^2 + \beta_{ac}^2 + \varepsilon_{ac}^2)a_0^2.$$

For zero incident angle $\varepsilon_{ac} = 0$, the wavenumber α_{ac} can be expressed as

$$\alpha_{ac} = \frac{\omega \cos\theta_z}{(U_0 \cos\theta_z \pm a_0)}.$$

Here $\theta_z = \tan^{-1}\left(\frac{\beta_{ac}}{\alpha_{ac}}\right)$ is the sweep angle and the plus sign corresponds to the fast moving wave and the minus sign corresponds to the slow moving wave. The corresponding phase speeds are $C = U_0 \pm \frac{a_0}{\cos\theta_z}$. The wavenumber for the fast moving wave is $\alpha_{ac} < \frac{\omega}{U_0 + a_0}$ and for the slow moving wave $\alpha_{ac} > \frac{\omega}{U_0 - a_0}$ and the sweep angle is limited by $\theta_z < \cos^{-1}\left(\frac{1}{M}\right)$. At $M = 3.5$ the sweep angle of the slow moving wave is limited to 73.39 degrees.

Table 2 Values of α_{ac} and wavelength for different spanwise wavenumbers

β_{ac}	α_{ac}	$\lambda_{ac,z}$ (in.)	$\lambda_{ac,x}$ (in.)	λ_x(in.)m=10 Neutral	λ_x(in.)m=20 Neutral
0.00	0.0198		0.2244		
0.01	0.0207	0.4440	0.2145		
0.025	0.0274	0.1776	0.1847		
0.05	0.0309	0.0888	0.1436		
0.10	0.0455	0.0444	0.0976		
0.15	0.0603	0.0296	0.0736		
				0.1951	0.2133

Table 2 gives the non-dimensional wavenumbers α_{ac}, β_{ac} and the dimensional wavelengths $\lambda_{ac,x}$, $\lambda_{ac,z}$ for the slow acoustic waves. The axial wavelengths for the neutral disturbances for the azimuthal

wavenumbers m = 10 and 20 are also given in the table. It is seen that the shortest possible spanwise acoustic wavelength is about 0.0296 inches and the corresponding axial wavelength is about 0.0736 inches. The wavelengths of the neutral disturbances are about 0.20 inches, which is about three times longer than the acoustic wavelength. Hence a conversion of both the spanwise wavelength and the axial wavelength has to occur to excite the instability waves inside the boundary layer.

Mean flow and transition for the Cone

Figure 4 shows the mean flow density contours computed using the WENO code. The figures 4(a-d) show the results for the cone at different nose radii r_0 = 0.001, 0.01 and 0.05 inches. The computations are performed at a unit Reynolds number of $1.0*10^6$/inch which yield Reynolds numbers based on the nose radius of 10^3, 10^4 and $5*10^4$. Figure 4(a) shows the density contours in larger domain while figures 4(b) and (c) show the flow field near the nose region. The leading edge shocks are located approximately at 0.0002, 0.002 in. and 0.02 inches upstream of the leading edge. The density profiles at different axial locations are plotted in Figs. 5(a)-(d) for the different bluntness cases r_0 =0.001, 0.01 inches in the physical and similarity coordinates. The compressible Blasius similarity profile is also included for comparison. The difference between the density profiles with the bluntness and the similarity profiles increases with the bluntness. For the bluntness case of r_0 =0.001 inches the boundary layer profiles approach the similarity profiles at about x = 2.0 inches while for the larger radius of 0.01 inches it approaches the similarity profiles at about 6.0 inches.

Figure 6 shows the growth rate and the N-Factors for the most amplified disturbances computed using the profiles obtained from the numerical solution for different bluntness r_0 = 0.001, 0.01, 0.05 inches. For comparison, the stability results for the Blasius similarity profiles, which model a sharp leading edge, are also shown in the figure. The frequency and the azimuthal wave number for the most amplified wave are about $F = 1.75*10^{-5}$ and m = 25 for the similarity profiles. For the smaller bluntness r_0 = 0.001 and 0.01 the N-Factor curves and the growth rate curves remain closer to the similarity curve. For the larger bluntness case r_0 = 0.05 the growth rates become smaller and the N-Factor curves move further to the right. The most amplified frequencies and the azimuthal wave numbers are $(1.75*10^{-5}, 25)$, $(1.75*10^{-5}, 25)$ $(0.60*10^{-5}, 25)$ for r_0 = 0.001, 0.01 and 0.05 inches respectively. This shows that the frequencies of the most amplified disturbances become smaller with increasing bluntness. The growth rate curves remain similar to the Blasius profile for all three bluntness cases. Boundary-layer transition data on a flat plate and on a cone, and free stream noise levels and the power spectral distribution of the free stream noise are presented in Ref. 9. The data shows the transition Reynolds number for a sharp cone in quiet conditions is about $9*10^6$. If this is used in the correlation to obtain the N-Factor at transition, then Fig. 6 gives an N-factor of 9.0 for a constant azimuthal wave number. The transition Reynolds numbers obtained using the N-factor of 9.0 for different bluntness cases are summarized in Table 3 and plotted in Fig. 7. The transition Reynolds number for blunt flat plates and blunt wedges were presented in Ref. 12 and are also included in the Fig. 7 and in the Table 3 for comparison. The ratio between the transition Reynolds number with bluntness and the transition Reynolds number for the similarity profile, $(Re_T)_b/(Re_T)_{Similarity}$, is about 1.05, 1.13, 2.10 respectively for $Re_r = 10^3$, 10^4, $5*10^4$. For the flat plate these factors are about 1.05, 1.30, 2.48, 3.49 respectively for $Re_b = 10^2$, 10^3, $5*10^3$, 10^4 and for the wedge these factors are 1.42, 7.01, 11.96 respectively for $Re_b = 10^3$, 10^4, $4*10^4$. This implies that the stabilizing effects of bluntness are much stronger in flows over flat plates and wedges than in flows over cones. Previous experiments[17, 18] and the stability calculations[19] showed that the transition Reynolds number for a blunt cone at a Mach number of 8 with nose Reynolds numbers of 30,000 increased by a factor of 1.7~2.0 compared to a sharp cone. This agrees with the calculations shown in the Table 3.

Table 3 Transition Reynolds number for the blunt flat plates, wedges and cones

Nose radius r_0 in.	Reynolds number based on nose radius	Transition location X (in.)			Transition Reynolds number $*10^6$			Ratio $(Re_T)_b/(Re_T)_{Similarity}$		
		Flat plate	Wedge	Cone	Flat Plate	Wedge	Cone	Flat Plate	Wedge	Cone
0.0	0	11.00	10.40	9.37	11.00	10.40	9.37	1.00	1.00	1.00
0.001	10^3	14.12	14.38	9.80	14.12	14.38	9.80	1.30	1.42	1.05
0.01	10^4	38.37	73.00	10.60	38.37	73.00	10.60	3.49	7.02	1.13
0.01 (4 mil)	$4*10^4$		28.50			114.00			10.96	
0.05	$5*10^4$			19.60			19.60			2.10

Generation of instability waves from a harmonic source

The computer code was modified from the Cartesian coordinates to cylindrical coordinates. To validate and to investigate the generation and the evolution of instability waves in axi-symmetric boundary layers a simulation with a harmonic point source located on the surface is performed. A blowing/suction distribution in the form

$$v = v_{max} \sin^2\left(\frac{\pi(x - x_{start})}{(x_{end} - x_{start})}\right) \cos m\theta \sin(\omega t)$$

is prescribed for the radial velocity component across a narrow slot on the surface. Here x_{start}, x_{end} are the starting and ending locations of the slot, m is the azimuthal wavenumber, ω is the frequency and v_{max} is the maximum velocity non-dimensionalized by the free stream velocity. In the present computations x_{start} = 0.70 in., x_{end} = 0.80 in., $m = 10$, $F=2.00*10^{-5}$ and $v_{max} = 0.00001$. The boundary layer thickness at the axial location $x = 0.75$ inches is about 0.007 inches. Figure 8 shows the evolution of the unsteady density fluctuations generated by the harmonic point source at a fixed time. Figure 9a shows the instantaneous pressure fluctuations along the wall and Fig. 9b shows the amplitude of the pressure fluctuations along the wall in a log scale. Figure 9b also includes the results from the parabolized stability equations (PSE) computations obtained for the same mean boundary layer profiles. The figures clearly show the initial generation and the eventual exponential growth of the instability waves inside the boundary layer. The growth of the disturbances agrees very well with the PSE results about ten boundary layer thicknesses downstream of the source. Following the PSE results up to the location of the source, the initial amplitude of the instability waves near the source can be estimated. From these values the receptivity coefficients defined by the initial amplitude of the pressure fluctuations at the wall near the harmonic source non-dimensionalised by the maximum source velocity can be evaluated.

$$C_{recpt,p_{wall}} = \frac{(p_{wall})_n}{v_{max}} \tag{15}$$

The computed receptivity coefficient is

$$C_{recpt,p_{wall}} = 0.50$$

Figure 10 shows the eigenfunction distributions for the density, ρ, and the azimuthal velocity, w, obtained from the simulation and the PSE computation at the axial location $x = 2.0$ inches. The agreement between the simulation and the PSE is excellent.

Interaction of a three-dimensional acoustic wave with the axi-symmetric boundary layer.

After the mean flow is computed, three-dimensional plane acoustic disturbances are introduced at the outer boundaries. The simulations are performed for a non-dimensional frequency of $F=2.00*10^{-5}$ and for spanwise wavenumbers $\beta_{ac} = 0.05$ and 0.15. The amplitude of the acoustic wave is $p_{ac}/p_{\infty} = 1.0*10^{-6}$. The computations are performed for zero incident angles. Figures 11 (a) and (b) show the results for the evolution of the unsteady density fluctuations obtained from the simulation for the slow wave $\beta_{ac} = 0.15$ at a fixed time in the (x, z) and (x, y) planes respectively. It is to be noted that the azimuthal angle $\theta = 0$ degrees lies in the (x, z) plane and $\theta = 90$ degrees lies in the (x, y) plane. The constant phase lines in the (x, y) or $\theta = 90$ degree plane is perpendicular to the cone axis. Figure 12 depicts the unsteady density fluctuations in the cross plane (z, y) at an axial location $x = 0.5$ inches. It is interesting to see the scattering of the acoustic field by the cone and the different ways the flow field is perturbed along the $\theta = 0$ and 90 degrees lines. The constant phase lines are parallel to the surface in the $\theta = 0$ direction and the acoustic field basically glances the cone without much distortion. In contrast, the constant phase lines are diffracted by the cone in the $\theta = 90$ direction and the acoustic field is very much distorted. These observations will reflect the way the boundary layers are perturbed by the three-dimensional plane acoustic waves. It is to be noted that the acoustic disturbances in the outer part of the domain in fig. 11 are decaying due to lack of resolution in this region due to the expansion of the domain.

Figures 13 (a) and (b) show the plan view of the density fluctuations on the surface of the cone in $(x, r\theta)$ planes. Figure 13 (a) depicts the flow field between the azimuthal angles (-90, 90) degrees so $\theta = 0$ line is in the middle of the region and figure 13(b) depicts the field between (0, 180) degrees so $\theta = 90$ line is in the middle. As it is seen, the disturbances evolve differently along the $\theta = 0$ and 90 degrees lines. Figures 14(a)-(d) show the pressure fluctuations on the surface along different azimuthal directions $\theta = 0, 42, 70$ and 90 degrees. Along the $\theta = 0$ line, the wavelength remains the same as the acoustic field up to $x = 1.5$ inches and it gradually starts to increase downstream. However, along the $\theta = 90$ degree line the wavelength increases starting from the leading edge and the disturbance amplitude starts to increase beyond $x = 1.5$ inches. It is also seen that the wavelength modulation and the amplitude growth spreads in the azimuthal direction as the disturbances evolve downstream.

Figure 15 shows the pressure fluctuations on the surface along the azimuthal direction at a fixed time at different axial stations $x = 0.10, 0.25, 0.50. 1.24$ and 2.00 inches. The figure shows that near the nose, $x = 0.1$ inches, the variation in the azimuthal direction is similar to a simple cosine wave and near $x = 0.25$ inches small wavelength disturbances start to appear in the middle region $\theta = 90$. Further downstream, the wavelengths or the number of waves m increases and these small wavelength disturbances spread towards $\theta = 0$ and 180 degrees. To investigate how the disturbances are evolving, a Fourier analysis is performed in the azimuthal direction. The disturbances are decomposed into the following form.

$$p(x,r,\theta,t) = \left\{ \sum_{m=-M}^{M} \tilde{p}_m(x,r)e^{im\theta} \right\} e^{-i\omega t} + c.c$$

Figure 16 shows the amplitude of the Fourier component $\left|\tilde{p}_m(x,r)\right|$ as a function of the azimuthal wavenumber m for the pressure distribution on the surface of the cone at different axial locations $x = 0.042, 0.27, 0.52, 1.00, 1.49, 2.72$ inches. As was discussed earlier, the spectrum is narrow and is concentrated near m = 0 for small x values and it widens as the axial distance increases. The amplitudes of the disturbances with azimuthal wavenumbers in the range of 8 to 12 start to increase beyond $x = 1.0$ inches. Figure 17 shows the variation of the amplitude of the spectrum $\left|\tilde{p}_m(x,r)\right|$ along the axial direction x for different $m = 0$, 10 and 20. The figure shows that the amplitude of the disturbances with $m = 0$ decreases and the amplitude for $m = 10$ increases sharply up to $x = 0.5$ inches and plateau up to $x = 1.0$ inches and increases exponentially downstream. However, the disturbance with high azimuthal wavenumber $m = 20$ increases first and then decreases with increasing axial distance. The linear stability analysis predicted that the azimuthal wavenumbers for the unstable waves range between 5 to 30. It is not clear why the disturbances with large m values are not amplified but the disturbances with m values in the range of 6 to 14 are amplified. Figure 17 also includes the results from the parabolized stability equations (PSE) computations obtained for the same mean boundary layer profiles. The figure clearly shows the eventual exponential growth of the instability waves inside the boundary layer. However, the initial amplitude of the instability waves is very small compared to the free stream acoustic disturbances. The initial amplitude from the PSE computations at x = 0.62 inches is about $5.0*10^{-9}$ compared to the free stream acoustic disturbance amplitude of $1.0*10^{-6}$. Hence, the receptivity coefficient is very small value $5.0*10^{-3}$.

Similar to the previous case, figure 18 show the plan view of the density fluctuations on the surface of the cone in $(x, r\theta)$ planes for the case $\beta_{ac} = 0.05$. Figure 18 (a) depicts the flow field between the azimuthal angles (-90, 90) degrees and figure 18(b) depicts the field between (0, 180) degrees. The observations are similar to the previous case with the disturbances evolve differently along the $\theta = 0$ and 90 degrees lines. Figures 19(a) and (b) show the pressure fluctuations on the surface along the different azimuthal directions $\theta = 0$ and 90 degrees. Surprisingly the disturbances did not grow along the $\theta = 90$ degree as was observed in the previous case with large $\beta_{ac} = 0.15$. These questions need further investigation.

Discussion and Conclusions

The boundary layer receptivity process due to the interaction of three-dimensional slow and fast acoustic disturbances with a blunt 5-degree cone and the evolution of disturbances inside the boundary layer are numerically investigated at a free stream Mach number of 3.5 and at a high Reynolds number of 10^6/inch. Both the steady and unsteady solutions are obtained by solving the full Navier-Stokes equations using the 5th-order accurate weighted essentially non-oscillatory (WENO) scheme for space discretization and using third-order total-variation-diminishing (TVD) Runge-Kutta scheme for time integration.

The results show that bluntness has a less stabilizing effect on the stability of the axi-symmetric boundary layers compared to two-dimensional boundary layers. The transition Reynolds number for the cone increases slowly up to a nose Reynolds number of 10000 and increases sharply at higher nose Reynolds numbers. This suggests that up to a nose Reynolds number of 10000, the cone could be assumed as a sharp cone for the stability analysis. The transition Reynolds number for a flat plate with leading edge thickness of 0.01 inches is about 3.5 times larger than that for the Blasius boundary layer, it is about 7.2 times for the wedge and it is about 1.13 times for the cone. Even at a very high nose Reynolds number of 50,000 this ratio is 2.1 for the cone.
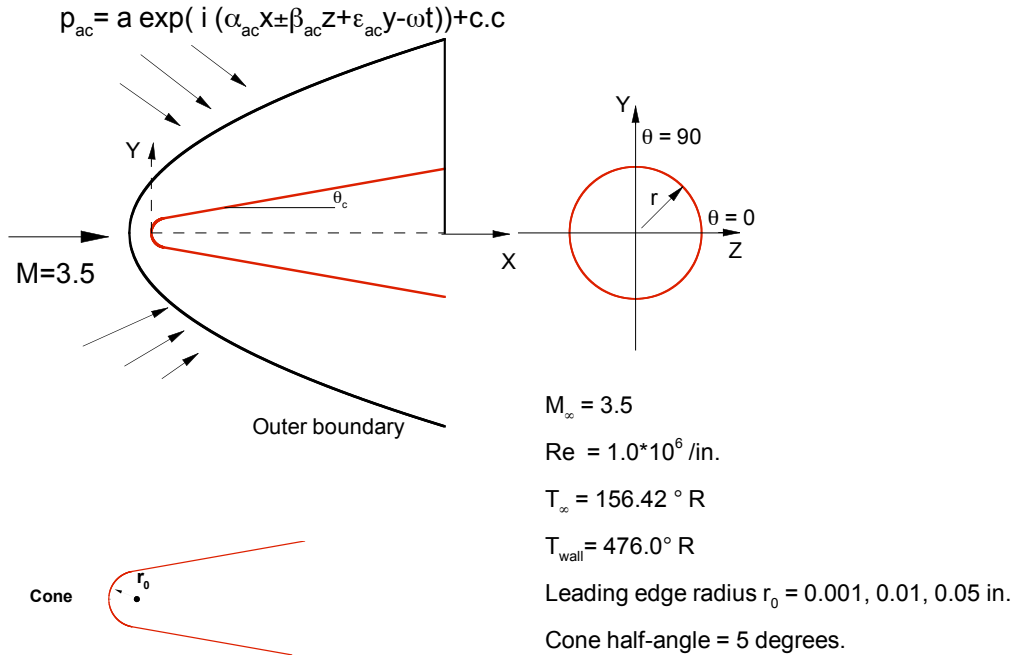
The unsteady simulations revealed that the interaction of a three-dimensional plane acoustic wave with a cone perturbed the flow field inside the boundary layer differently depending on the azimuthal direction. In regions where the constant acoustic phase lines are parallel to the surface the disturbances have the

same wavelength as the acoustic waves. In the regions where the constant phase lines are perpendicular to the surface the boundary layer is highly perturbed. The axial wavelengths of the disturbances increase and disturbances with high azimuthal wavenumbers appear in this region. Further downstream, these disturbances spread in the azimuthal direction. The amplitude of the excited disturbances is very small compared to the free stream acoustic disturbances. The receptivity coefficient is about $5.0*10^{-3}$. The simulation with high spanwise acoustic wavenumber showed that these high azimuthal wavenumber disturbances generated near the nose region become the instability waves and grow exponentially downstream. However, the simulation performed with the small spanwise acoustic wavenumber did not show any instability waves even though the modulation of the disturbances near the nose region appear similar. Another point of concern is that according to the linear stability analysis the disturbances with azimuthal wavenumbers in the range of 5 to 30 are unstable at the Reynolds number investigated in this paper. However, the simulation showed that the disturbances with high azimuthal wavenumbers of 20 did not amplify. These question will be investigated further.

References

1. Mack, L. M., "Boundary Layer Stability Theory", JPL 900-277 Rev. A, Nov. 1969, Jet Propulsion Lab., Pasadena, Calif.

2. Mack, L. M., "On the application of linear stability theory and the problem of supersonic boundary-layer transition," *AIAA Journal.*, 13, No. 3, 1975.

3. Gaponov, S. A., "Interaction between a supersonic boundary layer and acoustic disturbances," *Fluid Dynamics*, 6, 1977.

4. Gaponov, S. A., "Excitation of Instability Waves in the Supersonic Boundary Layer by Sound," *IUTAM Symposium Potsdam*, Springer-Verlag, 1993.

5. Gaponov, S. A. and Smorodsky, B. V., "Supersonic Boundary Layer Receptivity to Streamwise Acoustic Field," *IUTAM Symposium*,, Spinger-Verlag, 1999.

6. Fedorov, A. V., and Khokhlov, A. P., " Excitation of Unstable Modes in a Supersonic Boundary Layer by Acoustic Waves," *Fluid Dynamics*, No. 9, pp. 456-467, 1991.

7. Fedorov, A. V., and Khokhlov, A. P., "Sensitivity of a Supersonic Boundary Layer to Acoustic Disturbances," *Fluid Dynamics*, No. 27, pp. 29-34, 1992.

8. Sakaue, S., Asia, M., and Nishioka, M., "On the Receptivity process of supersonic laminar boundary layer", Laminar Turbulent Transition, Heidelberg, Springer-Verlag, 2000.

9. Fedorov, A. V., "Receptivity of High Speed Boundary Layer to Acoustic Disturbances," *AIAA Paper 2002-2846*, 2002.

10. P. Balakumar, "Transition in a Supersonic Boundary layer Due to Roughness and Acoustic Disturbances," *AIAA Paper 2003-358*9, 2003.

11. P. Balakumar, "Transition in a Supersonic Boundary layer Due to Acoustic Disturbances," *AIAA Paper 2005-0096*, 2005.

12. P. Balakumar, "Stability of a Supersonic Boundary layer Over Blunt Wedges," *AIAA Paper 2006-0137*, 2006.

13. Chen, F. J., Malik, M. R., Beckwith, I. E., "Comparison of Boundary Layer transition on a Cone and Flat Plate at Mach 3.5," *AIAA-88-0411*, 1988.

14. Shu, Chi-Wang, " Essentially Non-Oscillatory and Weighted Essentially Non-Oscillatory Schemes for Hyperbolic Conservation Laws," *NASA/CR-97-206253 and ICASE Report* N0. 97-6

15. Atkins, H. L., "High-Order ENO Methods for the Unsteady Compressible Navier-Stokes Equations," *AIAA Paper 91-1557*, 1991.

16. Balakumar, P., Zhao, H., and Atkins, H., "Stability of Hypersonic Boundary_layers Over a Compression Corner," *AIAA Paper* 2002-2848, 2002.

17. Potter, J. L., "Boundary-Layer Transition on Supersonic Cones in an Aeroballistic Range," *AIAA Journal.*, 13, No. 3, 1975.

18. Stetson, K. F., Thompson, E. R., Donaldson, J. C., and Siler, L. G., "Laminar Boundary Layer Stability Experiments on a Cone at Mach 8, Part 2: Blunt Cone," AIAA 22nd Aerospace Sciences Meeting, Reno, Nevada, January 9-12, *AIAA Paper 84-0006*, 1984.

19. Malik, M. R., Spall, R. E., and Chang, C. L., " Effect of Nose Bluntness on Boundary Layer Stability and Transition," *AIAA Paper 90-0112*, 1990.

$p_{ac}= a \exp(i \, (\alpha_{ac}x\pm\beta_{ac}z+\varepsilon_{ac}y-\omega t))+c.c$

$M=3.5$

θ_c

Outer boundary

Y

$\theta = 90$

r

$\theta = 0$

X

Y

Z

$M_\infty = 3.5$

$Re = 1.0*10^6$ /in.

$T_\infty = 156.42 \,°$ R

$T_{wall}= 476.0°$ R

Leading edge radius $r_0 = 0.001, 0.01, 0.05$ in.

Cone half-angle = 5 degrees.

Cone

r_0

Figure 1. Schematic diagram of the computational model.

(a)

wave angle
0
45
60
70

F

$\sqrt{Re_x}$

(b)

N Factor

BETA = 0.035 F=1.25E-5
BETA = 0.045 F=1.50E-5
BETA = 0.050 F=2.00E-5
BETA = 0.060 F=2.50E-5
BETA = 0.060 F=3.00E-5

$\sqrt{Re_x}$

(c)

N Factor

m = 20 F=1.50E-5
m = 20 F=2.00E-5
m = 20 F=2.50E-5
m = 20 F=3.00E-5
m = 10 F=2.00E-5
m = 0 F=2.00E-5

$\sqrt{Re_x}$
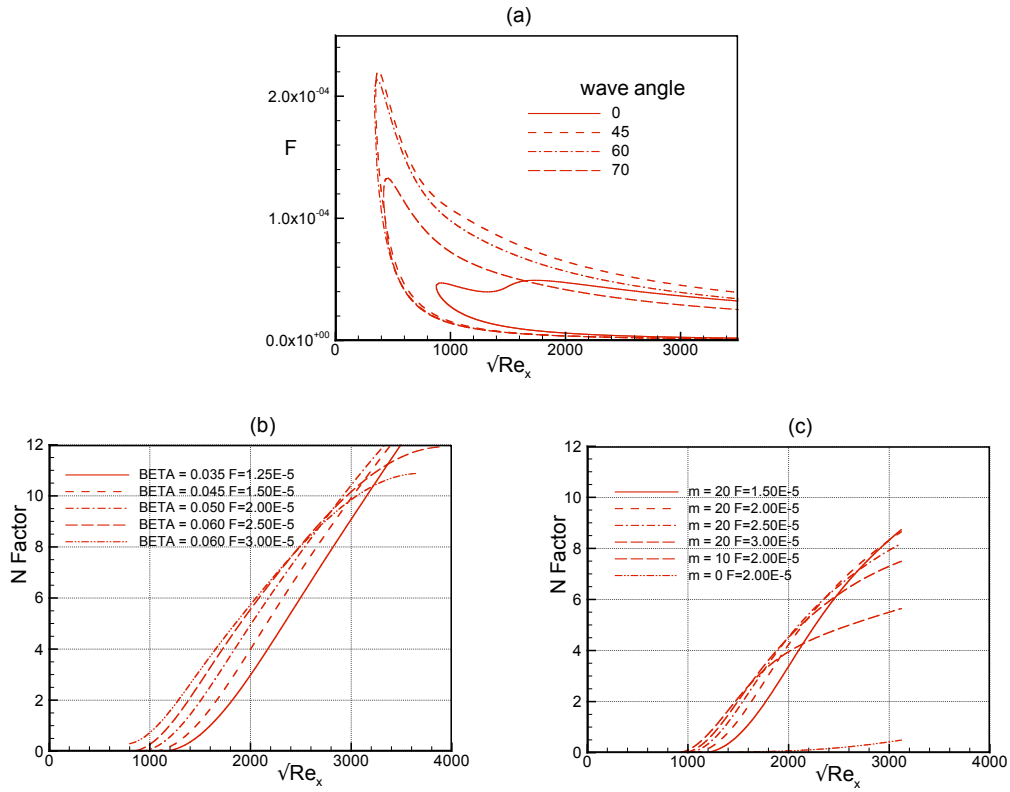
Figure 2. Neutral stability (a) and N-Factor diagrams (b), (c) for the boundary layer over a 5-deg cone. $M_\infty = 3.5$.
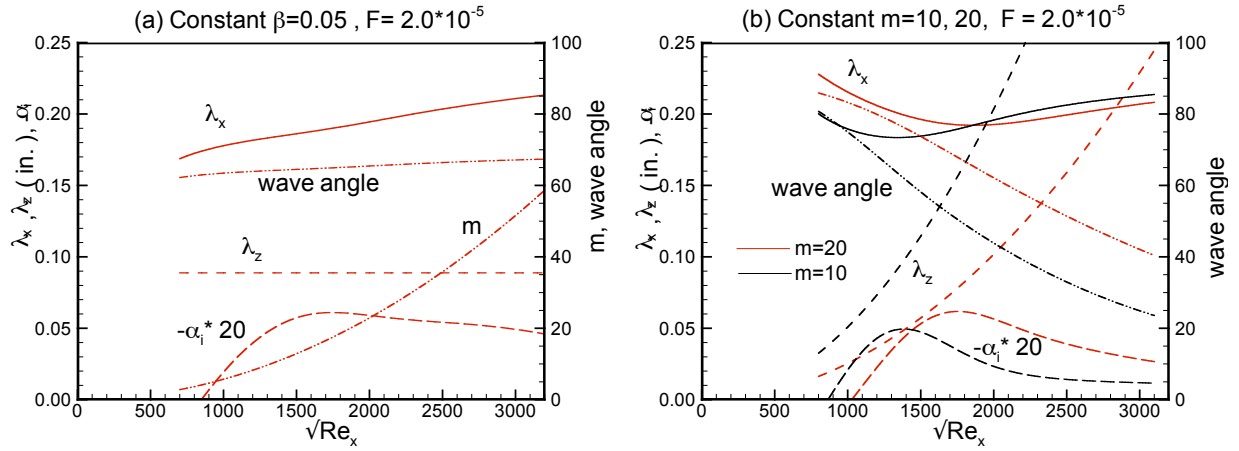
Figure 3. Variation of the axial and spanwise wave lengths, the growth rates and the azimuthal wave numbers for the most amplified wave $F = 2.0*10^{-5}$. (a) constant $\beta=0.05$, (b) constant m =10, 20.
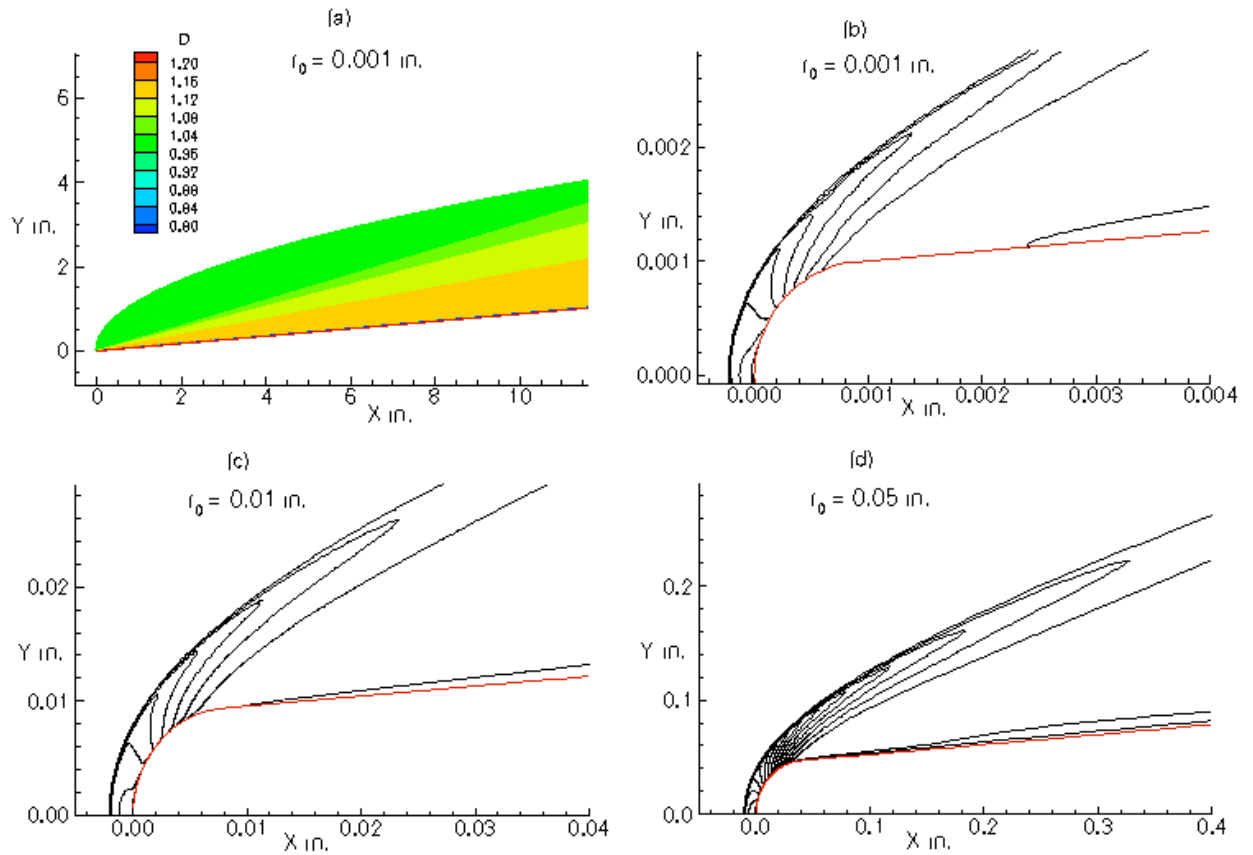
Figure 4. Contours of the density for flow over a 5-degree cone with a blunted leading edge at M=3.5
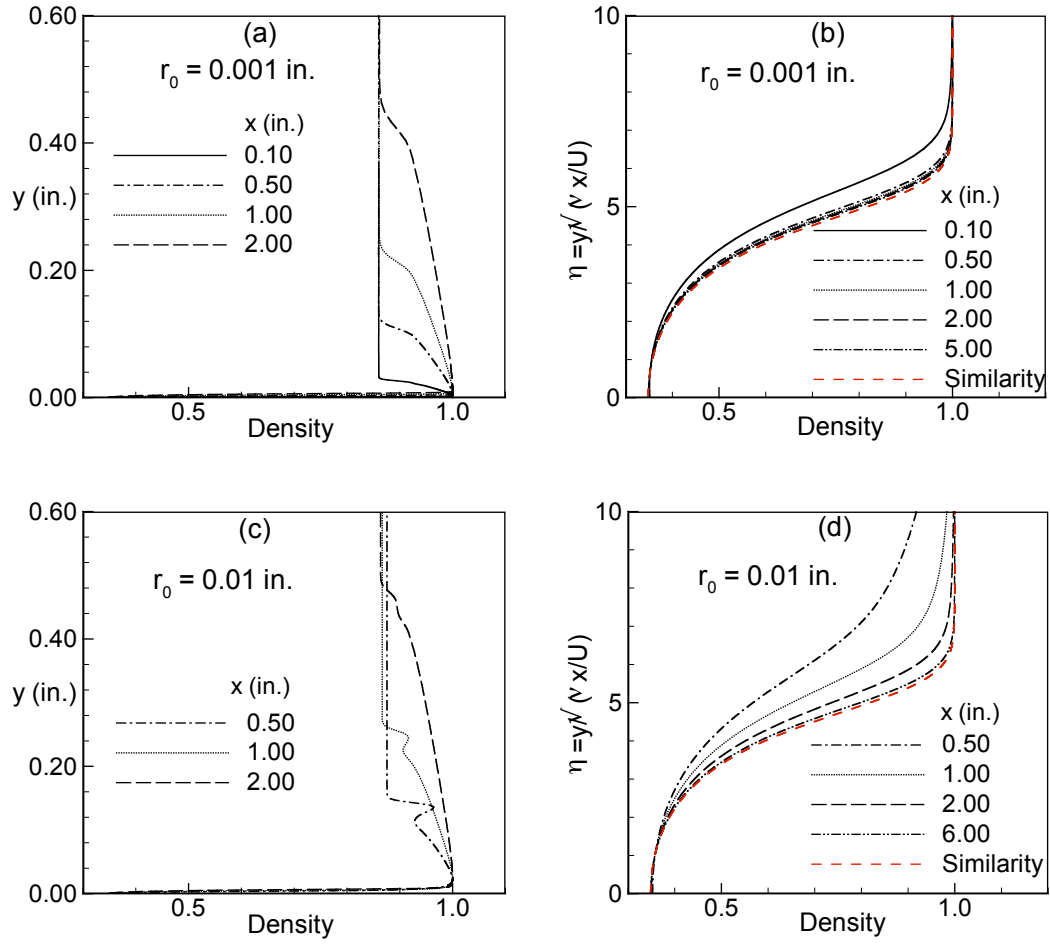
Figure 5. Mean density profiles at different X locations.
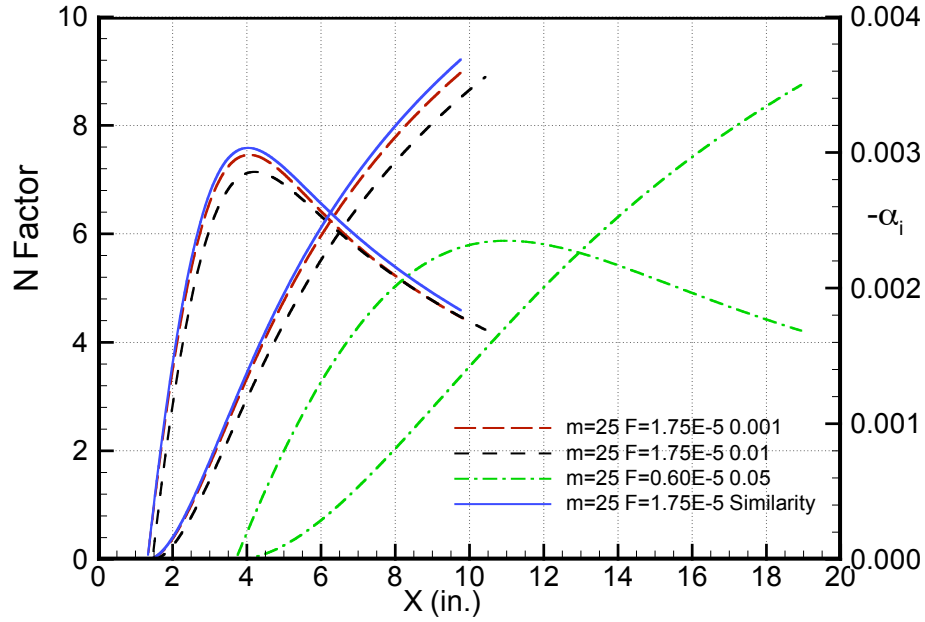
Figure 6. N-Factors and the growth rates for the most amplified disturbances for different bluntness r_0 = 0.001, 0.01, 0.05 in. at M = 3.5.
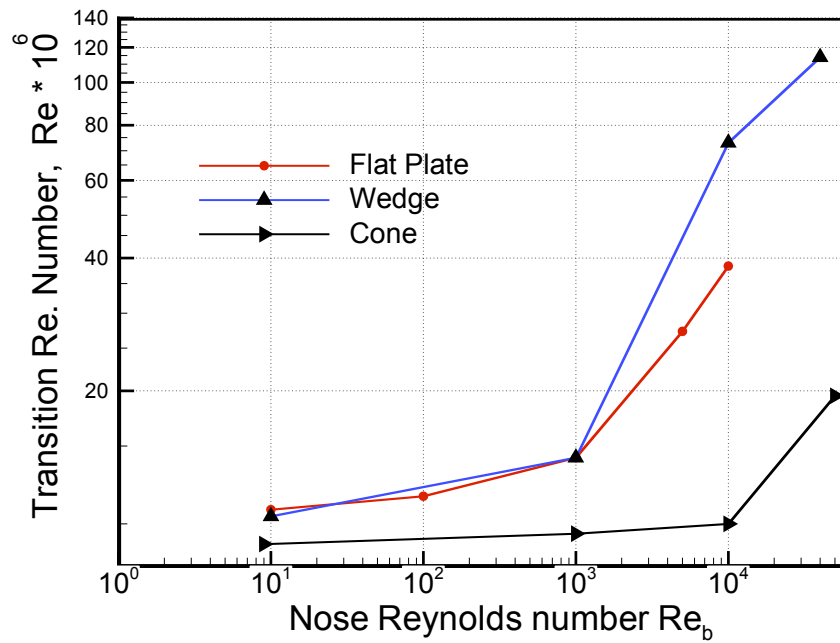
Figure 7. Transition Reynolds number for the flat plate and the wedge for different bluntness b = 0.0001, 0.001, 0.005, 0.01 in. at M = 3.5.
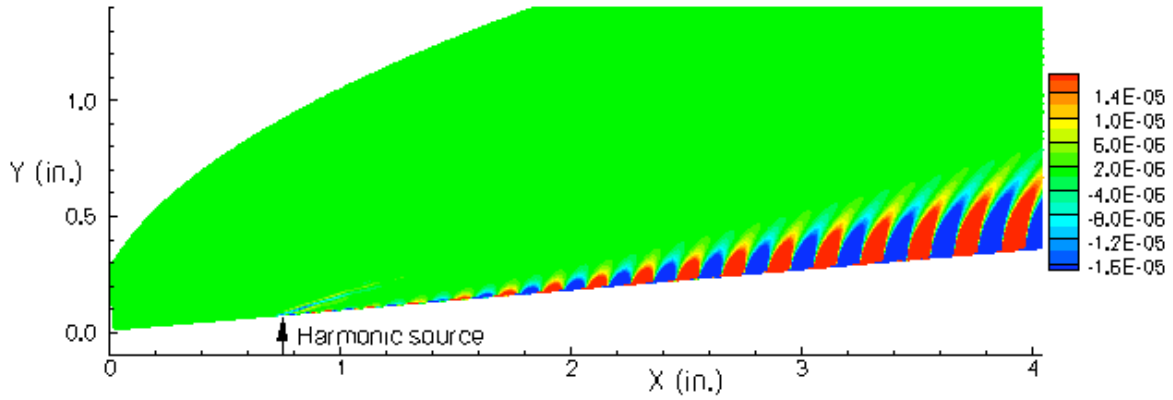
Figure 8. Contours of the unsteady density fluctuations due to a harmonic point source at $x = 0.75$ inches. $F=2.0*10^{-4}$, $m= 10$.
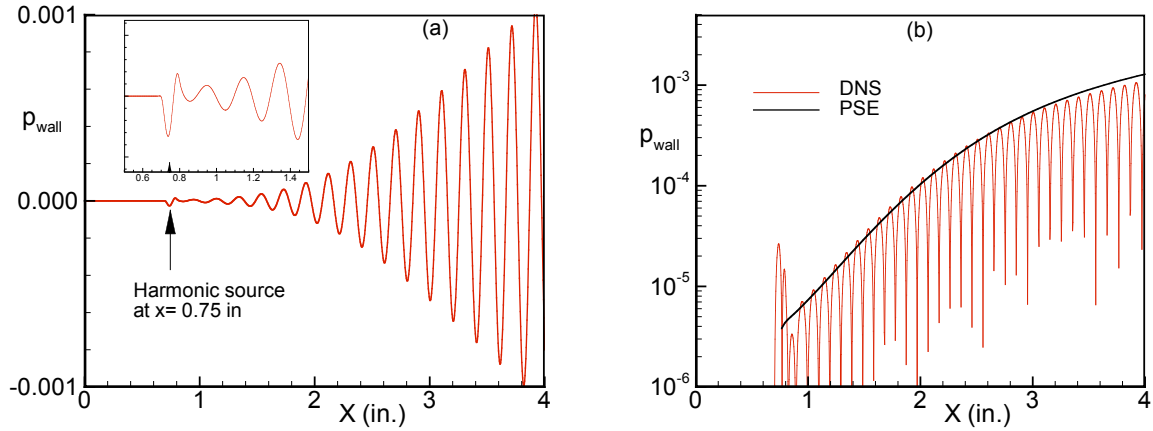
Figure 9. Amplitude of the pressure fluctuation at the wall and comparison with the PSE. $F=2.0*10^{-4}$, $m = 10$, $r_0 = 0.001$ inch.
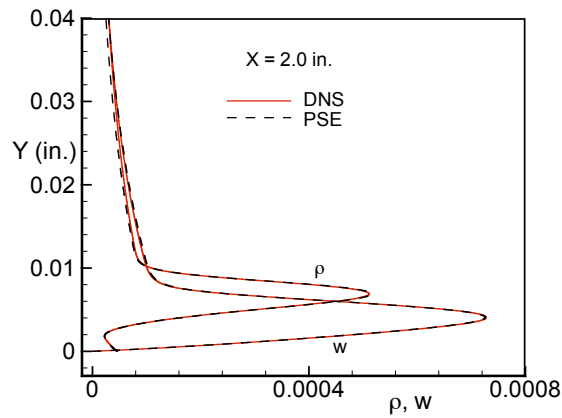
Figure 10. Eigenfunctions for the density and azimuthal velocity fluctuations and comparison with the PSE calculations at $X= 2.0$ inches. $F=2.0*10^{-4}$, $m = 10$, $r_0 = 0.001$ inch.
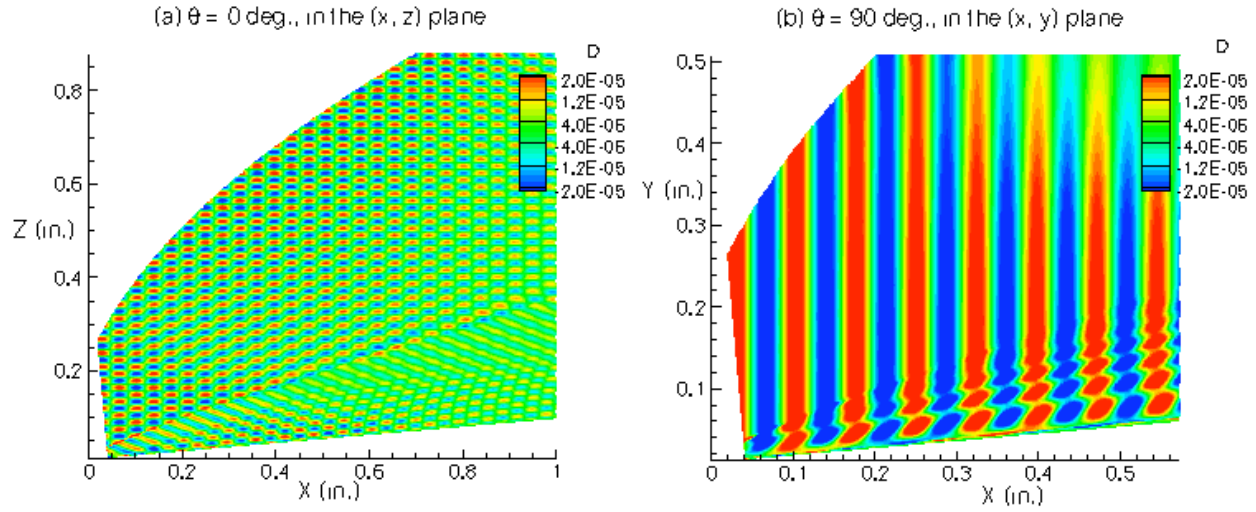
Figure 11. Contours of the unsteady density fluctuations due to the interaction of a 3D slow acoustic wave with a 5-deg cone with a blunted leading edge. $F = 2.00*10^{-5}$, $\beta = 0.15$, incident angle 0.0.
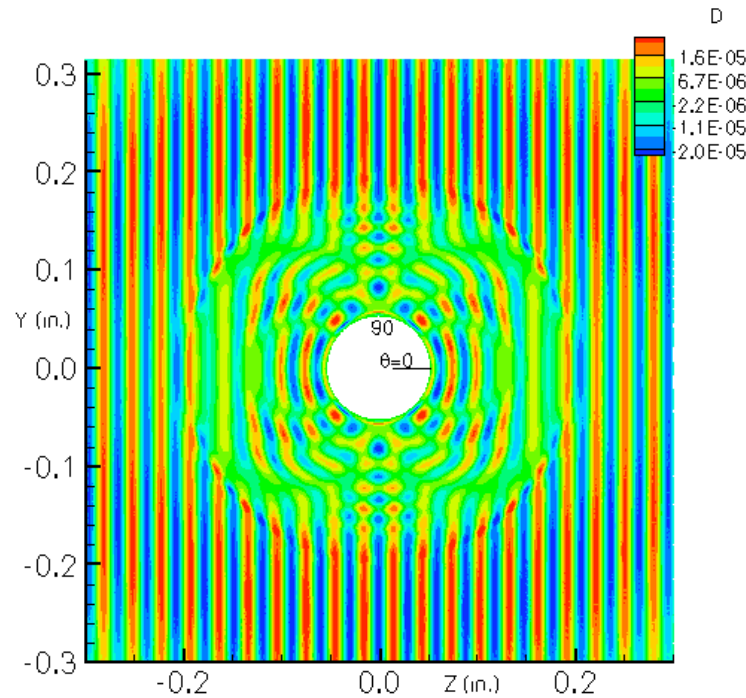
Figure 12. Contours of the unsteady density fluctuations in the y_z plane at $x = 0.5$ in. due to the interaction of a 3D slow acoustic wave with a 5-deg cone with a blunted leading edge. $F = 2.00*10^{-5}$, $\beta = 0.15$.

American Institute of Aeronautics and Astronautics
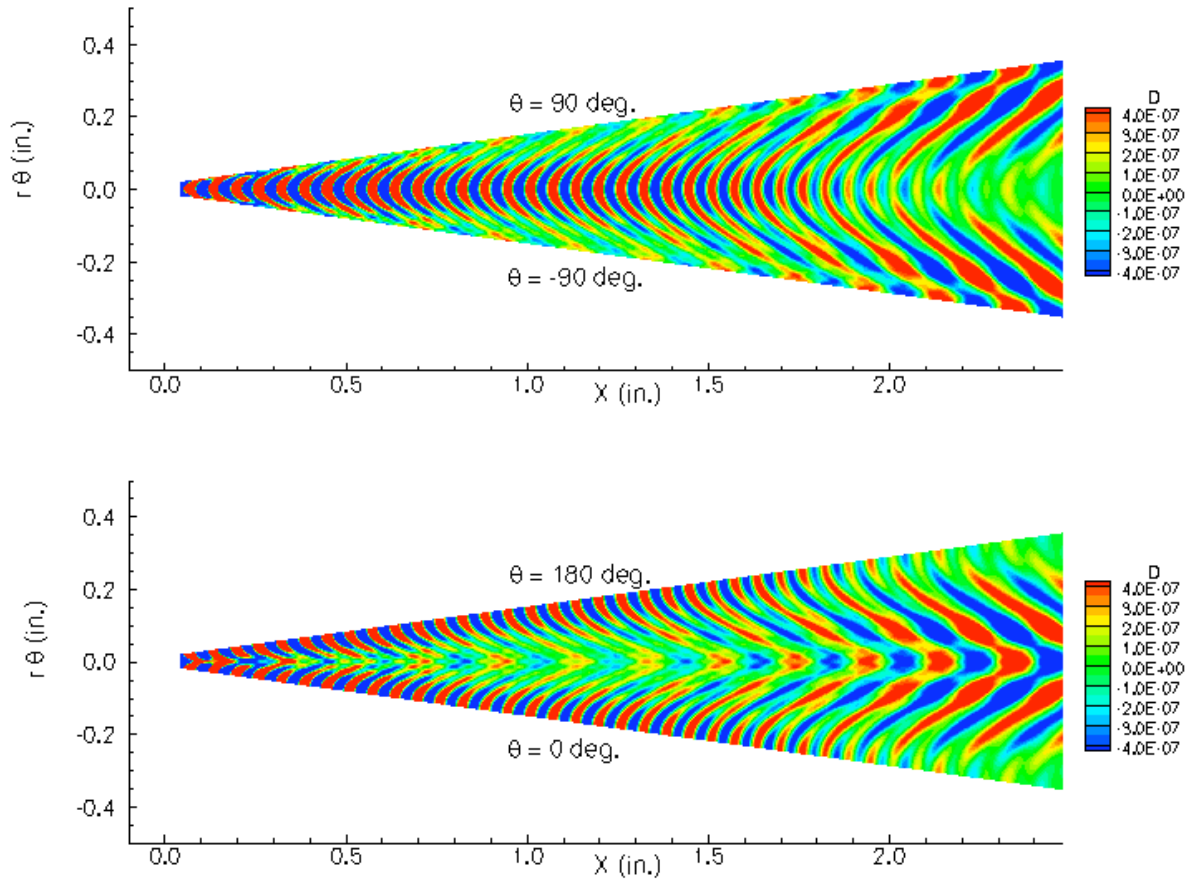
Figure 13. Contours of the unsteady density fluctuations due to the interaction of a 3D slow acoustic wave with a 5-deg cone with a blunted leading edge in the (x, rθ) plane. $F = 2.00*10^{-5}$, $\beta = 0.15$.
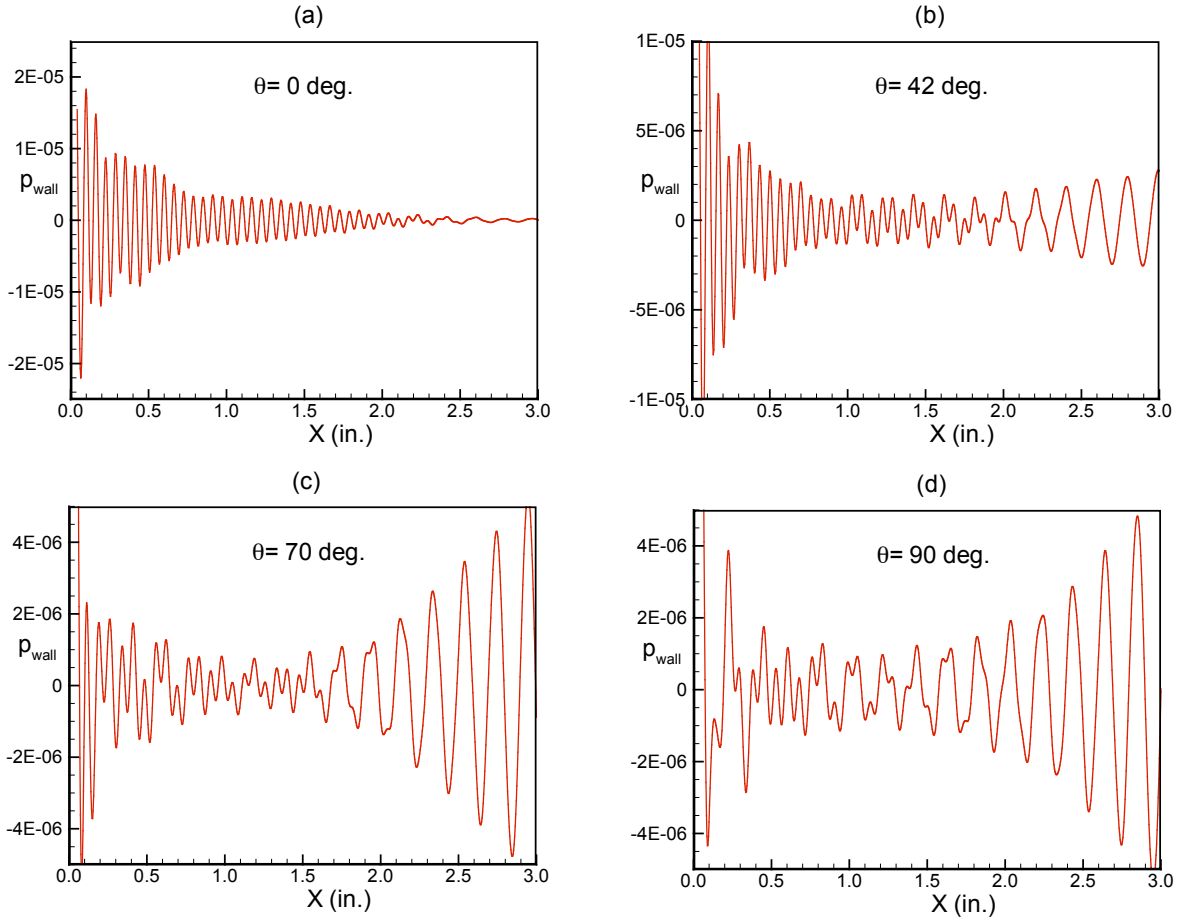
Figure 14. Pressure fluctuations on the wall along different azimuthal angles. $r_0 = 0.01$ in. $F = 2.00*10^{-5}$, $\beta = 0.15$.
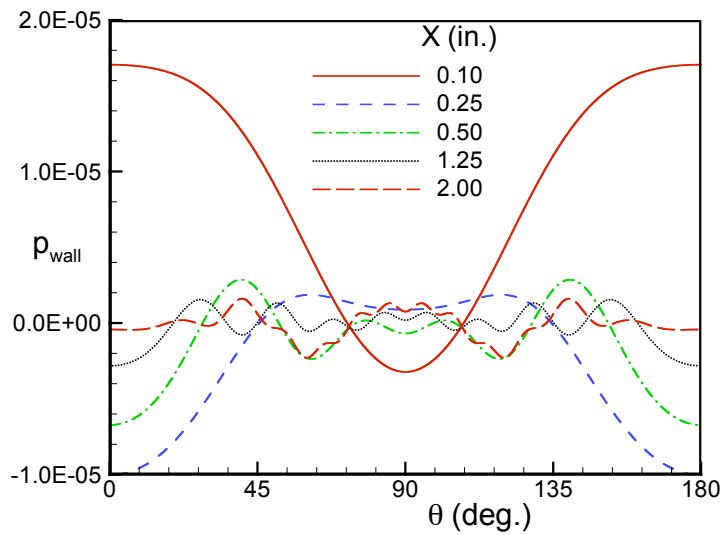
Figure 15. Pressure fluctuations on the wall at a fixed time along the azimuthal direction at different axial locations. $r_0 = 0.01$ in., $F = 2.00*10^{-5}$, $\beta = 0.15$.

American Institute of Aeronautics and Astronautics
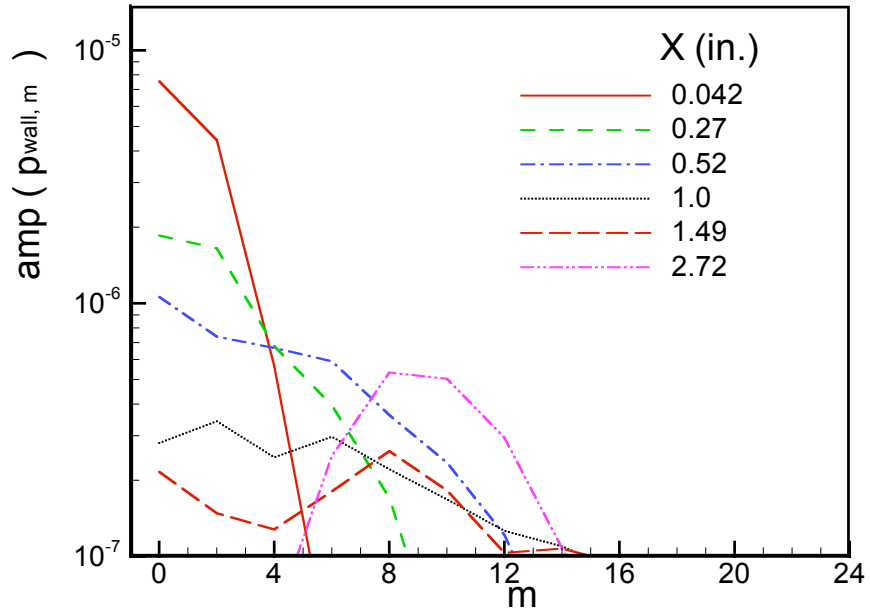
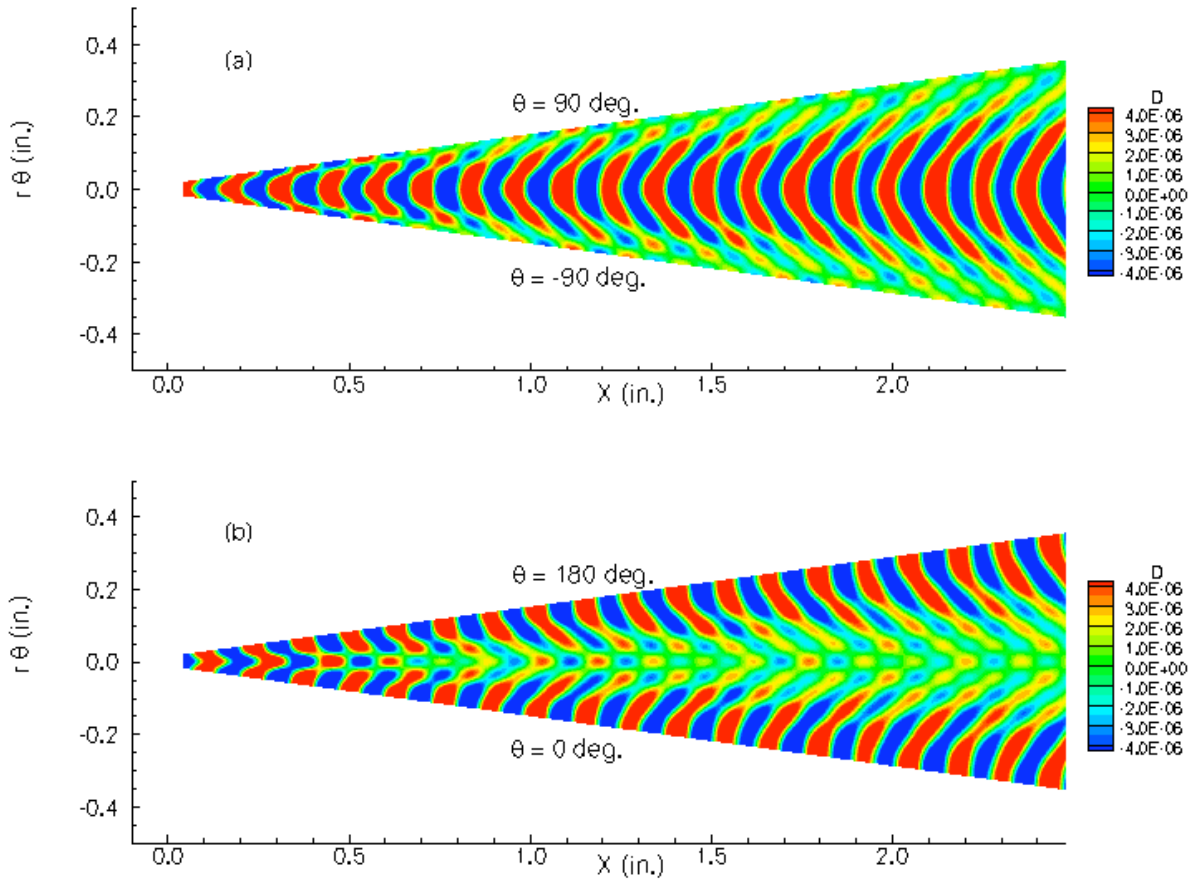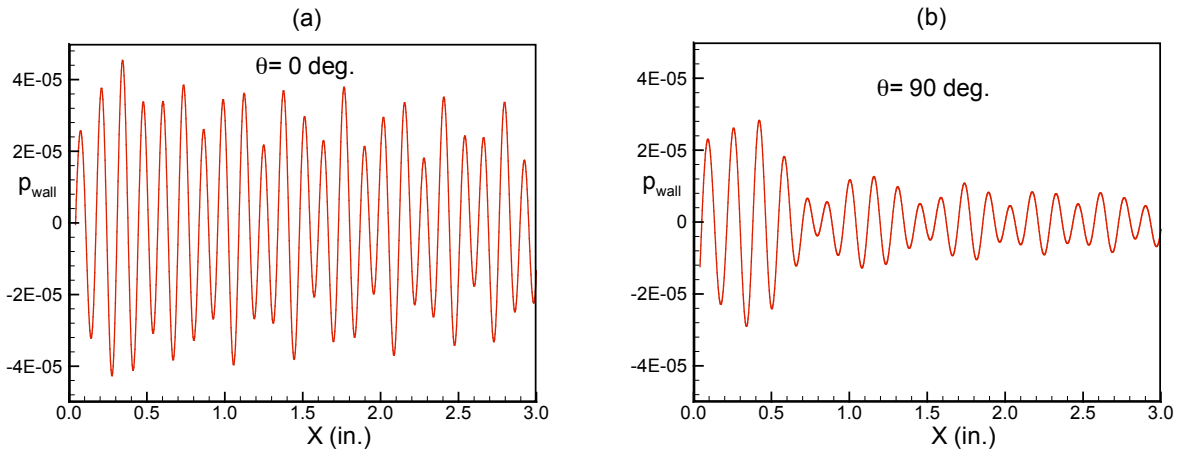**Figure 16. Spectral distribution at different axial locations. $F = 2.00*10^{-5}$, $\beta = 0.15$.**
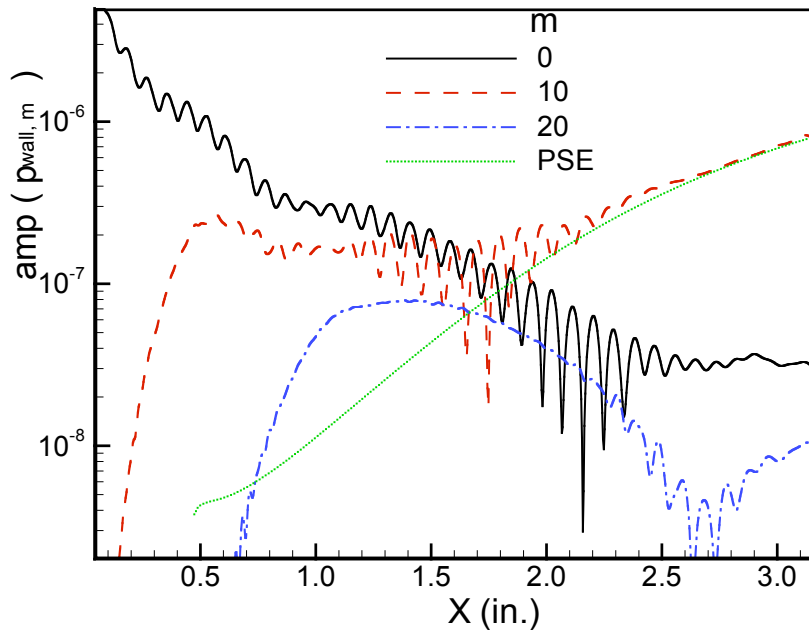
Figure 17. Variation of the amplitude of the spectrum along the axial direction for different m. $F = 2.00*10^{-5}$, $\beta = 0.15$.

Figure 18. Contours of the unsteady density fluctuations due to the interaction of a 3D slow acoustic wave with a 5-deg cone with a blunted leading edge in the (x, rθ) plane. $F = 2.00*10^{-5}$, $\beta = 0.05$.

Figure 19. Pressure fluctuations on the wall along different azimuthal angles $r_0 = 0.01$ in. $F = 2.00*10^{-5}$, $\beta = 0.05$.